



pubs.acs.org/acsaenm Article

# Nanoplastics Removal from Water using Metal—Organic Framework: Investigation of Adsorption Mechanisms, Kinetics, and Effective Environmental Parameters

Sweta Modak, Medha Kasula, and Milad Rabbani Esfahani\*



Cite This: ACS Appl. Eng. Mater. 2023, 1, 744-755



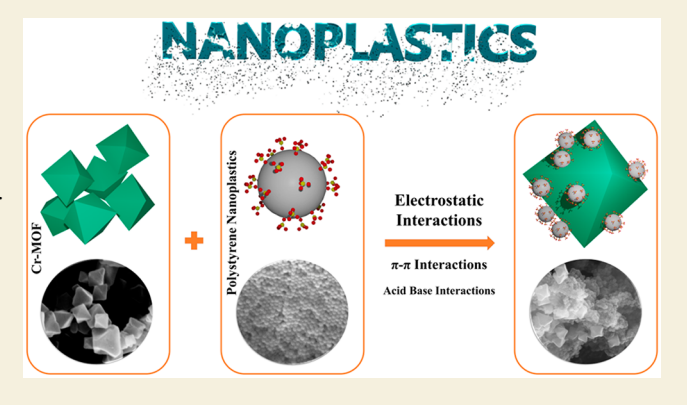
**ACCESS** I

III Metrics & More

Article Recommendations

s Supporting Information

**ABSTRACT:** Nanoplastics are becoming a concern for the environment and are gaining significant attention due to their challenging removal process and ability to transport coexisting pollutants. Because of their mobility, small size (<1  $\mu$ m), and accumulation tendency, nanoplastics are toxic for terrestrial and aquatic living organisms and humans, causing inflammation and oxidative stress. In this study, we investigated the removal of polystyrene nanoplastics (PSNPs) from water using a chromium-based metal—organic framework (Cr-MOF/MIL-101). Cr-MOF was synthesized via a hydrothermal method using chromium nitrate and terephthalic acid and characterized via different analytical approaches. A 96% removal efficiency was achieved with initial concentrations of 5 and 70 ppm and adsorption kinetics followed the pseudo-first-order model. The adsorption isotherm at



room temperature was best fitted with the Freundlich adsorption model, and the maximum adsorption capacity of 800 mg/g was achieved. The electrostatic interaction between PSNPs and Cr-MOF was the most dominating mechanism responsible for adsorption. The Cr-MOF showed acceptable regeneration capacity for cyclic removal of PSNPs.

**KEYWORDS:** nanoplastics, microplastics, MOFs, water treatment, plastic pollution

# 1. INTRODUCTION

Plastics have vast applications owing to their versatile qualities like high stability, low density, and low cost. These qualities are responsible for the increased global demand for plastics and further increased global production, which was more than 381 million metric tons in 2019.<sup>2,3</sup> The increased production and use of plastics have increased the plastic waste generated globally to more than 242 million tons in 2016. However, plastics have low biodegradability; even then, they may get shredded into smaller pieces generating micron- and nanosize plastics. Micro-/nanoplastics can be generated through two primary and secondary sources. Primary sources include the micro/nanoplastics that are synthesized originally for applications like abrasive agents and exfoliants in cosmetics, etc.<sup>6</sup> However, secondary sources include the micro/nanoplastics generated through fragmentation and degradation of larger particles.

In addition to the lack of biodegradability, nanoplastics can act as adsorbents for other toxic pollutants like heavy metals, pesticides, and antibiotics, which make them highly toxic. <sup>10–13</sup> Nanoplastics are potentially more dangerous than microplastics because their smaller size enables them to pass through cell membranes and may create toxicological effects on their surroundings and pose a risk to humans harming gastro-

intestinal tract and kidney functions. <sup>14–18</sup> Among the various types of nanoplastics, polystyrene is one of the most used plastics for manufacturing CDs, toys, styrofoam (food containers and packing products), automobile parts, laboratory ware, and office supplies. <sup>19</sup> Polystyrene (PS) provides around 90% of the world's plastic needs and is commonly prevalent in the environment. <sup>20</sup> In this regard, the negative effects of nano size and micron size PS on living organisms have been reported by researchers. <sup>21,22</sup> Also, polystyrene nanoplastics (PSNPs) showed resistance in destabilizing compared to other nanoplastics, making their removal more challenging. <sup>23</sup>

Several cutting-edge methods, such as membranes, agglomeration, electrocoagulation, and traditional activated sludge, can potentially remove micro-/nanoplastics, but these sectors are still in need of in-depth investigation to be sophisticated for the acceptable removal of nano- and microplastics.<sup>24–28</sup>

Received: October 20, 2022 Accepted: December 28, 2022 Published: January 27, 2023





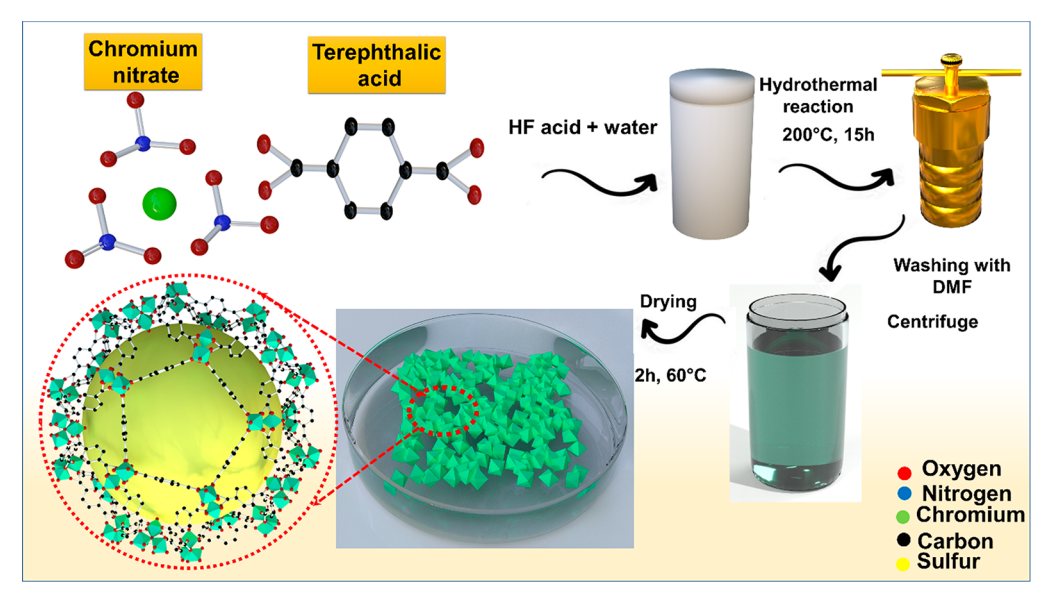


Figure 1. Synthesis process for Cr-MOF through a hydrothermal reaction at 200 °C for 15 h.

Additionally, these technologies have certain unavoidable drawbacks, such as high energy requirements, inability to handle small-sized (micro-/nanoplastics) pollutants, challenging scaling-up process, and lack of reproducibility.<sup>29</sup> Therefore, there is a great need to investigate new methods for the effective removal of nanoplastics. Among these methods, adsorption can be considered a possible approach to removing micro-/nanoplastics from water due to its gentle working conditions, lower energy consumption, and negligible byproducts. Carbon-based materials (such as granular activated carbon<sup>30</sup> and CuNi carbon material<sup>31</sup>) and layered double hydroxides<sup>32</sup> have been researched as potential adsorbents for the removal of nanoplastics from water. However, these adsorbents lack functionality toward different types of nanoplastics and have deficient adsorption capacity. Metalorganic frameworks (MOFs) are porous, crystalline materials constructed by the assembly of metal ions and organic ligands, which showed great performance in various applications like gas storage, separation, catalysis, sensing and contaminant removal, etc.<sup>33-38</sup> Owing to the high porosity, tunable structure, and rich functionality, MOFs show promising properties such as structural and surface tunability as a potential adsorbent for nanoplastics removal from water. 39-41 Previous research has demonstrated the use of Zr-based-MOFs (UiO-66-OH@MF-3) and Co-based-MOFs (ZIF-67) for the removal of micro-/nanoplastics. However, these MOFs showed limited adsorption capacity (about 34.5 mg/g) toward micro-/nanoplastics. 42,43

Hence, we report using Cr-based-MOFs for efficient removal of polystyrene nanoplastics (PSNPs) from water with enhanced adsorption capacity. We report complete isotherm adsorption experiments, including equilibrium study and kinetic study, at different concentrations of PSNPs and varying operating conditions. We also comprehensively investigate the adsorption mechanism of PSNPs on Cr-MOF.

# 2. EXPERIMENTAL SECTION

#### 2.1. Materials

The polystyrene nanoparticles were obtained from Polysciences (Warrington, PA, USA), with a slight anionic surface charge from the sulfate ester groups. Chromium nitrate (98.5%), terephthalic acid

(>99%), and  $N_{\nu}$ , are acquired from VWR (Radnor, PA, USA). All the chemicals were used without purification.

# 2.2. Synthesis of Cr-MOF

The Cr-MOF was successfully synthesized by the hydrothermal method according to the literature with slight changes.  $^{44}$  Briefly, 0.83 g of terephthalic acid and 2 g of chromium nitrate were mixed in 70 mL of water. Next, 0.15 mL of hydrofluoric acid was added to the mixture under stirring conditions at room temperature and stirred for 15 min. This mixture was then transferred into an 80 mL Teflon-lined autoclave and heated in the oven at 200  $^{\circ}\mathrm{C}$  for 15 h. After cooling the autoclave to room temperature, the mixture was washed with  $N_{r}N_{r}$  dimethylformamide three times and dried in the oven at 60  $^{\circ}\mathrm{C}$  for 12 h, and fine green powder was collected. The synthesis process of Cr-MOF is shown in Figure 1.

# 2.3. Characterization

Fourier transform infrared (FTIR) spectroscopy (AVATAR, Thermo Nicolet, spectrophotometer) was used to study the functional groups and covalent bonds in the PSNPs and Cr-MOF before and after adsorption. The crystallinity of Cr-MOF was studied using X-ray diffraction (XRD) patterns, acquired with Cu K $\alpha$  radiation (Bruker D8, Advance X-ray powder diffractometer) and Co Klpha radiation (Bruker D8, Billerica) at 298 K and at  $2\theta$  ranging from 0 to 40°. The Brunauer-Emmett-Teller (BET) surface area, pore size, and pore volume of Cr-MOF were analyzed by an ASAP 2020 (Micromeritics) at a pretreatment temperature of 110 °C. The  $\zeta$  potentials of PSNPs and Cr-MOF at different pHs were measured using a Nano ZS zetasizer (Malvern Pan-analytical, Malvern). The surface morphology of PSNPs and Cr-MOF before and after adsorption was investigated using scanning electron microscopy (ThermoFisher Scientific APREO). All the samples were gold-coated using gold sputtering before SEM analysis to avoid the charging of samples by the electron beam. The elemental composition of all the materials was examined via energy-dispersive X-ray spectroscopy (EDX) (ThermoFisher Scientific APREO).

#### 2.4. Adsorption Process

A stock solution of 100 ppm of PSNPs was prepared by diluting the original commercial solution (2.5% w/v concentration) with MiliQ water and sonicated for 20 min in a sonication bath. The adsorption of PSNPs on Cr-MOF was carried out at ambient temperature (25 °C). The effect of adsorption conditions like pH of the solution, contact time, and adsorbate concentration on the adsorption capacity of Cr-MOF was studied. Aqueous solutions of PSNPs of two different concentrations (5 and 70 ppm) were prepared by diluting the stock

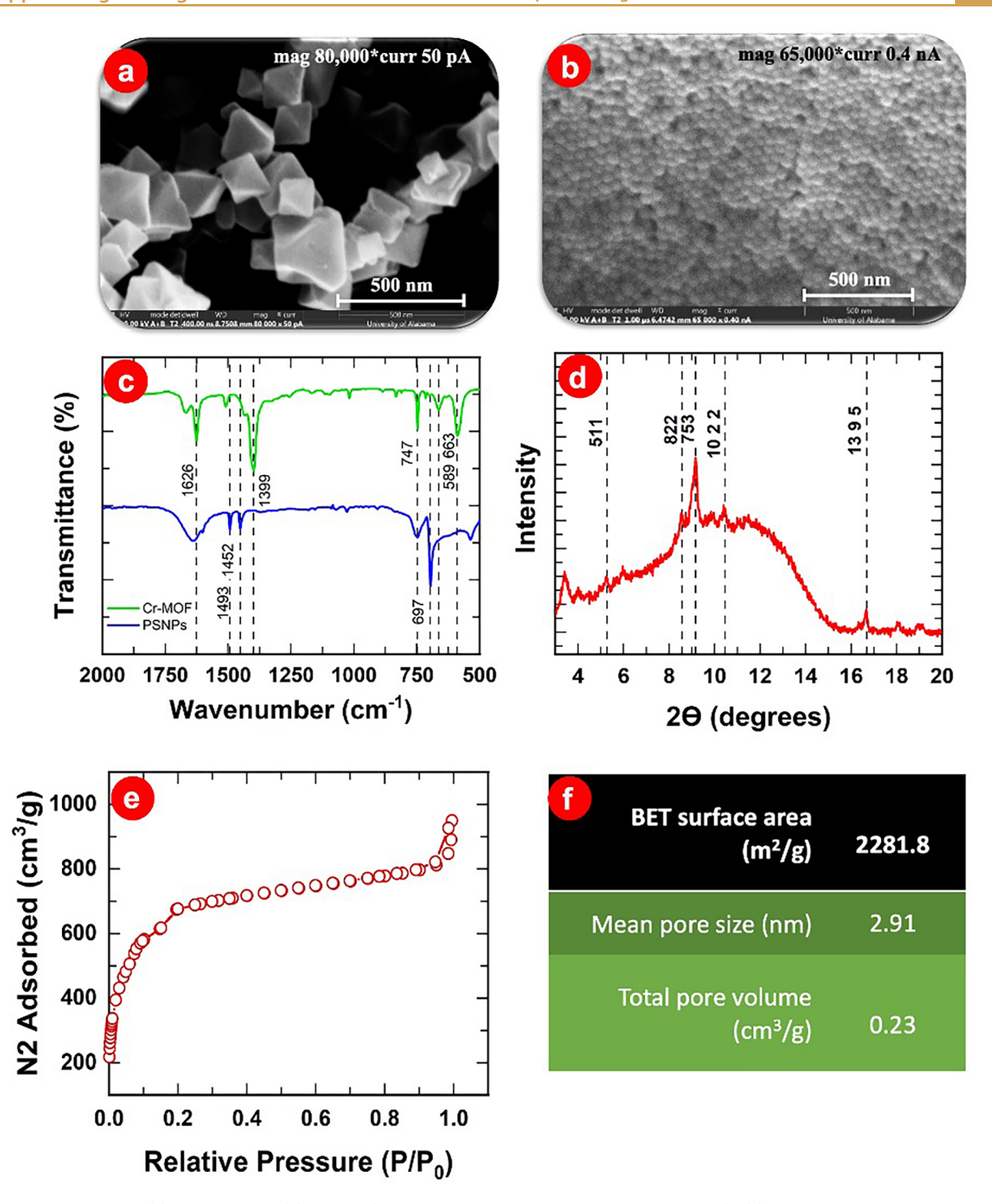


Figure 2. SEM images of (a) Cr-MOF and (b) PSNPs (samples were gold-coated before SEM analysis). (c) FTIR of PSNPs and Cr-MOF. (d) XRD pattern of Cr-MOF. (e) N<sub>2</sub> adsorption—desorption of Cr-MOF (BET). (f) BET analysis of Cr-MOF.

solution for pH and kinetics studies. A specific amount (4 mg) of the Cr-MOF was added to 40 mL of the PSNPs solution, followed by stirring at 220 rpm for 24 h. The pH value of each solution was adjusted from 2 to 10 using 0.1 M NaOH or 0.1 M HCl solution. The solution was filtered after 24 h adsorption using a syringe filter, and the final concentration of PSNPs in the filtrate was measured with a UV—vis spectrophotometer at a wavelength of 254 nm. This wavelength was obtained depending on the full spectrum scanning (200–800 nm) of the solution using UV—vis. The adsorption capacity of Cr-MOF was calculated using the following formula:

$$q = \frac{C_0 - C_f}{W} \times V \tag{1}$$

where q is adsorption capacity (mg/g),  $C_0$  is the initial concentration of PSNPs (mg/L),  $C_f$  is the equilibrium concentration of PSNPs (mg/L), V is the volume (L), and W is the weight of Cr-MOF (g).

#### 2.5. Kinetic and Isotherm Models

To study the adsorption mechanism of PSNPs on Cr-MOF, the experimental data were fitted with different kinetic and isotherm models. Three different kinetic and isotherm models were investigated in this study. The Langmuir adsorption model indicates

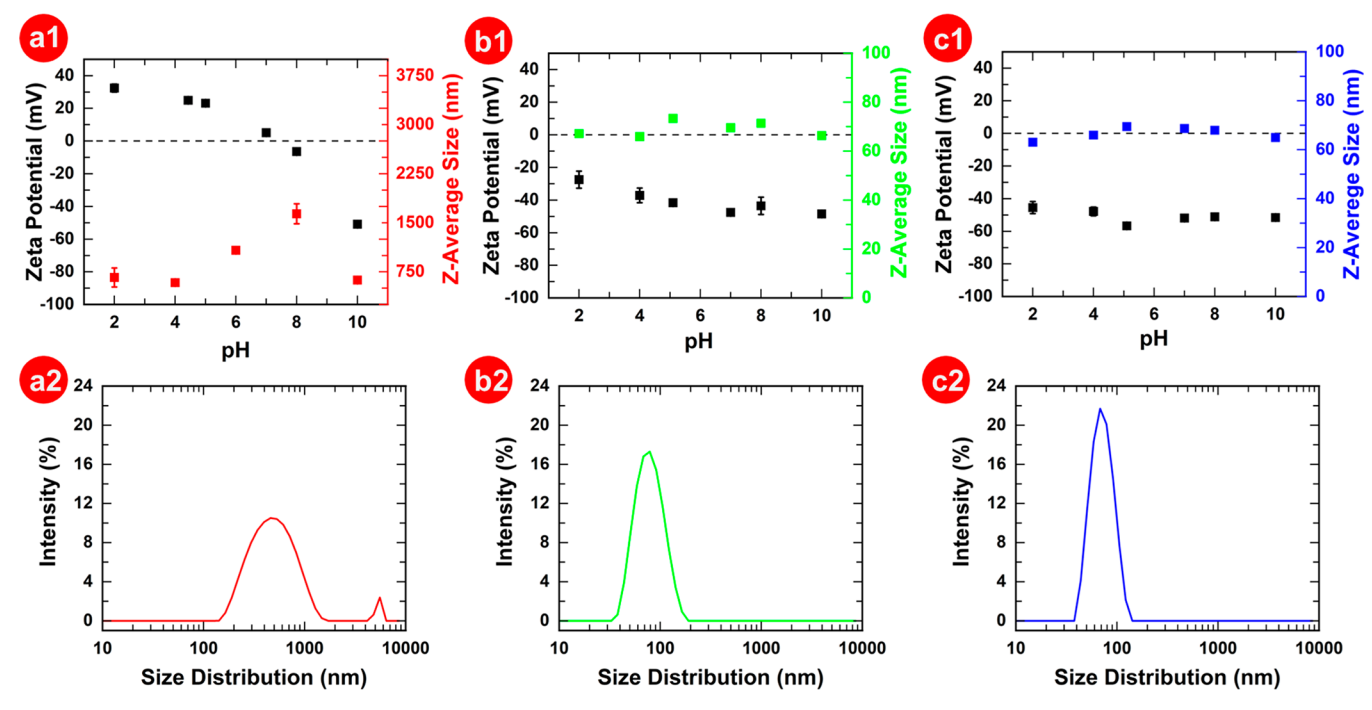


Figure 3.  $\zeta$  potential and size (z-average) of (a1) 100 ppm of Cr-MOF, (b1) 5 ppm PSNPs, and (c1) 70 ppm PSNPs at different pHs and T = 25 °C. Consistent  $\zeta$  potential for Cr-MOF at various pHs was obtained with a standard deviation of less than 2.5%. Intensity-based particle size distribution of (a2) 100 ppm of Cr-MOF, (b2) 5 ppm PSNPs, and (c2) 70 ppm PSNPs at their original pH = 5 and T = 25 °C.

a homogeneous monolayer adsorption process with a finite number of sites with an equal affinity toward adsorbate.<sup>45</sup> The nonlinear version of the Langmuir model is given by eq 2.

$$q_{\rm e} = \frac{Q_{\rm o} K_{\rm L} C_{\rm e}}{1 + K_{\rm L} C_{\rm e}} \tag{2}$$

where  $K_{\rm L}$  is the Langmuir constant that relates the affinity of adsorbate toward active sites (L/mg),  $C_{\rm e}$  is the equilibrium concentration of adsorbate (mg/L),  $Q_{\rm 0}$  is the maximum adsorption capacity (mg/g), and  $q_{\rm e}$  is the adsorption capacity at equilibrium (mg/g).

The Freundlich isotherm model assumes heterogeneous surfaces or distribution of active sites with varied affinities and stronger active sites are occupied first. The nonlinear version of the Freundlich isotherm can be expressed as

$$q_{\rm e} = K_{\rm F} C_{\rm e}^{1/n} \tag{3}$$

where  $K_{\rm F}$  is the Freundlich constant relating the adsorption capacity  $({\rm L}^{1/n}\,{\rm mg}^{1-1/n}\,{\rm g}^{-1})$  and 1/n is the adsorption intensity of the adsorbent (dimensionless).

The Temkin isotherm model directly considers the adsorbent and adsorbate interactions. This model assumes that the heat of adsorption declines linearly with the coverage of adsorbate molecules. <sup>47</sup> The linearized version of the Temkin isotherm model is as follows:

$$Q_{e} = B \ln K_{T} + B \ln C_{e} \tag{4}$$

where B = RT/b, B is the isotherm constant, R is the gas constant, T is the absolute temperature (K), b is related to the adsorption heat, and  $K_T$  is the Temkin isotherm equilibrium constant.

The pseudo-first-order (PFO) model suggests the physical adsorption of adsorbate and is widely applied for the adsorption in solid—liquid systems. The experimental data were fitted using the following equation:

$$\ln\frac{(q_{\rm e} - q)}{q_{\rm e}} = -k_1 t \tag{5}$$

where  $q_{\rm e}$  and q represent the adsorption capacity at equilibrium and at any time of the adsorption (mg/g), respectively,  $k_{\rm l}$  is the pseudo-first-order rate constant (min<sup>-1</sup>), and t is the time (s).

The pseudo-second-order (PSO) rate equation assumes chemical adsorption of adsorbates and second order adsorption of adsorbates onto the surface of the adsorbent.<sup>49</sup> The PSO equation is expressed as

$$q = \frac{q_e^2 k_2 t}{1 + q_e k_2 t} \tag{6}$$

where  $k_2$  is the pseudo-second-order rate constant.

The intraparticle diffusion model (IPD) was first presented by Webber and Morris (1963) and it only predicts the internal diffusion of the adsorbate. The IPD identifies the rate-limiting phases or mechanisms of the adsorption process and is expressed as <sup>50</sup>

$$q_{t} = K_{d}t^{0.5} + C (7)$$

where  $k_d$  is the IPD rate constant  $(mg/(g \cdot h^{0.5}))$  and C is a constant for any experiment (mg/g).

#### 2.6. MOF Regeneration Process

To study the regeneration of Cr-MOF, the exhausted MOF (Cr-MOF saturated with PSNPs) was regenerated with different solvents, including methanol (99.8% pure), ethanol (99.5% pure), and 0.005 M NaOH. The exhausted MOF was separated from the MOF-PSNPs mixture using a 0.1  $\mu$ m filter (Whatman Schleicher & Schuell). The separated MOF was then dispersed into the solvents and shaken for 15–20 min and separated using a 0.1  $\mu$ m filter. The separated MOFs were washed with plenty of DI water to remove the adherent solvents. After the regeneration of MOF with NaOH, the surface charge of the MOF was regained by adding 0.01 M HCl into the MOF-water solution until pH = 5 was achieved. After the complete desorption process, the MOF was dried in an oven for 2–3 h at 60 °C and used for the next adsorption cycle.

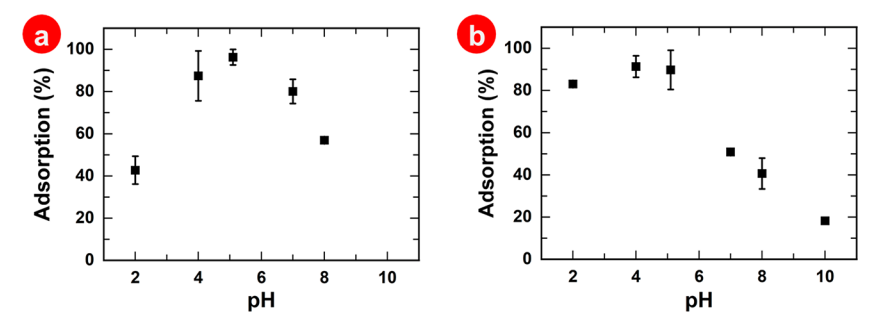


**Figure 4.** Adsorption performance of Cr-MOF toward (a) 5 ppm and (b) 70 ppm PSNPs at different pHs and constant temperature of 25 °C with the adsorbent concentration of 100 ppm. A maximum adsorption of more than 96% was obtained at pH 5 in both cases of initial concentration of PSNPs (5 and 70 ppm).

#### 3. RESULTS AND DISCUSSION

#### 3.1. Structural Characteristics

The SEM analysis was employed to examine the surface morphology of PSNPs and Cr-MOF (Figure 2a,b). Crystals of Cr-MOF with octahedral geometry<sup>51</sup> and spherical PSNPs nanoparticles were observed, as depicted in Figure 2a,b. The sizes of Cr-MOF crystals and PSNPs in the SEM images were 200–400 and 50–70 nm, respectively.

FTIR analysis of PSNPs and Cr-MOF examined the functional groups in the PSNPs and Cr-MOF (Figure 2c). The broad band observed at 3074, and 3325 cm<sup>-1</sup> represents the O-H stretching vibration of water adsorbed on the surface of Cr-MOF and PSNPs. Also, these bands represent the C-OH groups present in Cr-MOF. The FTIR of Cr-MOF showed peaks at 1399 cm<sup>-1</sup> due to the presence of O— C-O symmetric vibrations in COOH groups and at 1626 cm<sup>-1</sup> due to the C=C stretching of the benzene ring. The peak at the lowest wavenumber 589 cm<sup>-1</sup> was associated with Cr—O vibration in Cr-MOF. 52 There are three absorption peaks at the wavenumbers 1650, 1493, and 1452 cm<sup>-1</sup> due to the presence of aromatic C=C stretching vibration in benzene rings. The absorption peaks at the wavenumbers of 747 and 697 cm<sup>-1</sup> correspond to C—H out-of-plane bending vibration, which states the presence of only one substituent in the benzene ring. The XRD pattern of Cr-MOF is shown in Figure 2d and Figure S1. The five characteristics peaks at angles 5.27°, 8.57°, 9.18°, 10.46°, and 16.69° match with the literature, which confirmed the successful synthesis of Cr-MOF.<sup>53-55</sup> These angles were indexed to the indices (5 1 1), (8 2 2), (7 5 3), (10 2 2), and (13 9 5), similar to the previously reported literature. 56 The peaks observed at small angles characterize the mesoporous nature of MOF. The adsorption and desorption of N<sub>2</sub> on the Cr-MOF surface, as shown in Figure 2e, states that a type I adsorption isotherm was followed, suggesting monolayer adsorption on microporous solids. A small hysteresis loop at the higher relative pressure end is observed due to the presence of voids formed by crystal arrangements.<sup>57</sup> The BET surface area of Cr-MOF was 2281.8  $\pm$  137.2 m<sup>2</sup>/g, with a pore size of 2.91  $\pm$  0.34 nm and pore volume of  $0.23 \pm 0.05$  cm<sup>3</sup>/g (Figure 2f). These values are similar to previously reported values in the literature that confirmed the successful synthesis of Cr-MOF.<sup>58</sup>

Figure 3 shows the  $\zeta$  potential of Cr-MOF (100 ppm) and PSNPs (5 and 70 ppm) at different pHs. The  $\zeta$  potential of Cr-MOF was observed to decrease with increasing pH from 2 to 10 (Figure 3a)). The positive charge of Cr-MOF at pH = 5 was due to the unsaturated chromium ions present in the MOF.<sup>59</sup>

The point of zero charge (pH<sub>zcp</sub>) for Cr-MOF was observed at pH 7.5, similar to what was found in the literature. The  $\zeta$  potential of PSNPs decreased with increasing pH (Figure 3b1,c1). The negative charge on PSNPs throughout the pH range is due to the anionic charge on the surface of PSNPs from sulfate esters. Across the pH range of measurement, the change of  $\zeta$  potential values of 5 ppm PSNPs was slightly more noticeable compared with that at 70 ppm. This behavior may be due to the higher effect of H<sup>+</sup> and Cl<sup>-</sup> ions on the surface charge of PSNPs at a lower concentration.

The Z-average particle size of Cr-MOF obtained from DLS analysis was observed to vary with pH, ranging from around 600 to 1600 nm (Figure 3a1). The intensity-based particle size distribution of Cr-MOF measured at pH = 5 and T = 25 °C showed a size of around 500 nm, which matched the SEM image size observation (Figure 3a2). The increase in the particle size of Cr-MOF at pH 6 and 8 can be related to the  $\zeta$ potential of Cr-MOF in this pH range. Any particles with  $\zeta$ potential closer to the isoelectric point (pHzcp) are unstable and tend to agglomerate (approximately in the range +30 to -30 mV).<sup>62</sup> This must be the reason for the significant increase (from ~700 to ~1600 nm) in the particle size of Cr-MOF at pH 6 and 8, with  $\zeta$  potential ranging from +10 to -10 mV. The size of PSNPs was in the range 60-70 nm throughout the pH range and at both 5 and 70 ppm concentrations, which states the negligible effect of pH and concentration on the particle size of PSNPs. The intensitybased size distribution of both 5 and 70 ppm PSNPs showed a narrow size distribution of 40-100 nm (Figure 3b2,c2). No agglomeration of PSNPs was observed due to the higher stability of particles with  $\zeta$  potential less than -30 mV and higher electrostatic repulsion present between the particles.

# 3.2. Adsorption Mechanism

The adsorption of PSNPs on Cr-MOF was observed to be highly dependent on the pH. The maximum adsorption of more than 96% was obtained at pH 5 in both cases of initial concentration of PSNPs (5 and 70 ppm) (Figure 4). The adsorption trend shows the parabolic behavior by increasing adsorption from acidic pH 2 to pH 5, and then, a decrease of adsorption was noticed by increasing the pH from 5 to pH 10 for both 5 and 70 ppm initial concentrations of PSNPs. This behavior was due to the electrostatic interaction between PSNPs and Cr-MOF, which might be the primary adsorption mechanism. These results agree with the  $\zeta$  potential (Figure 3) measurements as discussed earlier. At pH 4 and 5, the negatively charged PSNPs and positively charged Cr-MOF promoted the electrostatic attraction and hence increased the adsorption. Whereas at pH 6–8, the  $\zeta$  potential of Cr-MOF is

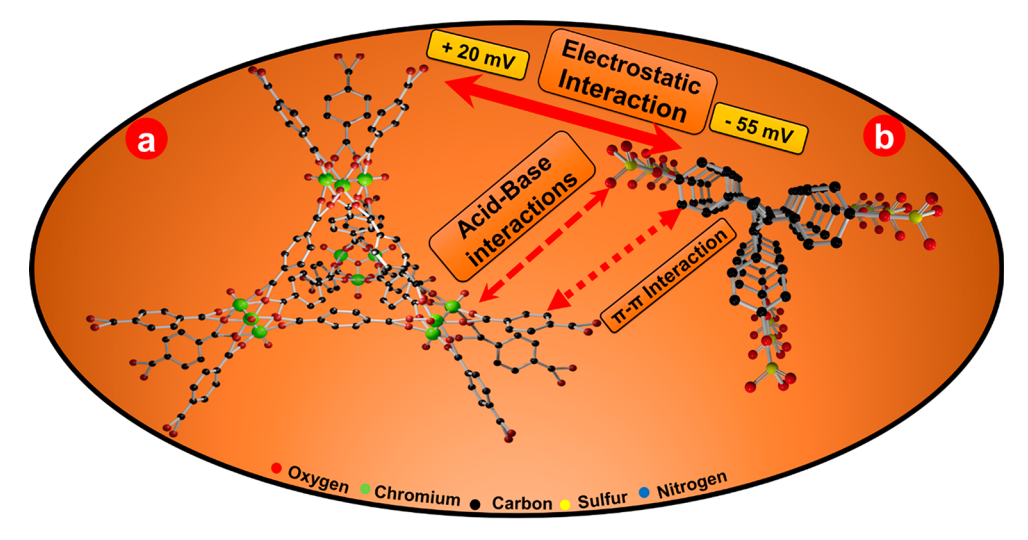


**Figure 5.** Molecular structure of (a) Cr-MOF and (b) PSNPs with sulfate ester functional groups. Three main mechanisms of electrostatic, acidbase, and  $\pi - \pi$  interaction are dominant adsorption mechanisms of PSNPs on Cr-MOF.



Figure 6. (a) FTIR analysis, (b1) SEM analysis, and (b2) EDX analysis of Cr-MOF after adsorption of PSNPs. Both analyses showed the existence of PSNPs on the Cr-MOF surface, confirming the adsorption of PSNPs on the surface of Cr-MOF.

closer to its isoelectric point, resulting in increased MOF particle size. This increased size of MOFs, i.e., aggregation, resulted in reduced interaction active sites of MOFs for PSNPs, reducing adsorption efficiency. In addition, the lower adsorption efficiency in this range of pH might be due to the lower positive surface charge of MOFs compared to acidic pH (Figure 3a1).

No significant adsorption was attained at pH 10 because at this pH the surface charge of MOF becomes negative and the PSNPs surface charge was negative, which caused repulsion between these two components. Higher adsorption (80%) was observed at pH 2 in the case of 70 ppm PSNPs compared to 40% adsorption for 5 ppm. This behavior might be due to the higher negative surface charge of 70 ppm (ZP = -45 mV) compared to 5 ppm (ZP = -25 mV) at pH = 2. Reduced adsorption was observed for both concentrations from pH = 5to pH = 2. This behavior might be justified based on the fact that the PSNPs have sulfate groups on the surface, which provided a negative surface charge at pH = 5. However, these sulfate groups showed lowered ionization at lower pH due to the presence of excess H+ ions. Hence, the electrostatic interactions between the Cr-MOF and PSNPs are reduced, and other adsorption mechanisms, such as acid-base interactions, became dominant.<sup>63</sup> Another explanation for this behavior might be the fact that the excess H<sup>+</sup> at acidic condition interact

with PSNPs and prevent the interaction between PSNPs and MOF.<sup>64</sup> The adsorption mechanisms involved in removing PSNPs using Cr-MOF are shown in Figure 5. Mainly, three types of adsorption mechanisms governed the adsorption, including (i) electrostatic interaction between the positively charged Cr-MOF and negatively charged PSNPs, (ii)  $\pi - \pi$  interactions of the benzene ring present in terephthalic acid of Cr-MOF and polystyrene,<sup>65–68</sup> and (iii) acid–base interactions of the chromium node and the sulfate ester group.<sup>63</sup>

FTIR, SEM, and EDX analyses were employed to examine the loaded Cr-MOF (Cr-MOF with adsorbed PSNPs) after 24 h of adsorption to obtain more detailed information about the adsorption process. The FTIR analysis of Cr-MOF after adsorption showed similar peaks to that of fresh Cr-MOF. Only one additional peak at wavenumber 697 cm<sup>-1</sup> was observed in the FTIR analysis of Cr-MOF after adsorption, stating the presence of PSNPs on the surface of Cr-MOF (Figure 6a). 69,70 The SEM analysis of Cr-MOF after adsorption has shown the PSNPs covering the surface of Cr-MOF (Figure 6b1). The EDX and EDX-EDS analysis of Cr-MOF after adsorption showed the presence of chromium from the Cr-MOF and sulfur from the sulfate groups present on the surface of PSNPs (Figure 6b2 and Figure S2). The presence of sulfur proves the adsorption of PSNPs on the surface of Cr-MOF, as sulfur was only present on the surface of PSNPs.

Table 1. Kinetics Parameters of Adsorption of PSNPs on Cr-MOF

Conc. (ppm)	Pseudo first ord	ler	Pseudo second order		
	$C_t = C_0$	$e^{-K_1t}$	$\frac{1}{C_t} = K_2 t + \frac{1}{C_0}$		
	K <sub>1</sub>	$\mathbb{R}^2$	$K_2$	$\mathbb{R}^2$	
5	0.558	0.97	1.783	0.41	
70	0.128	0.98	0.002	0.71	

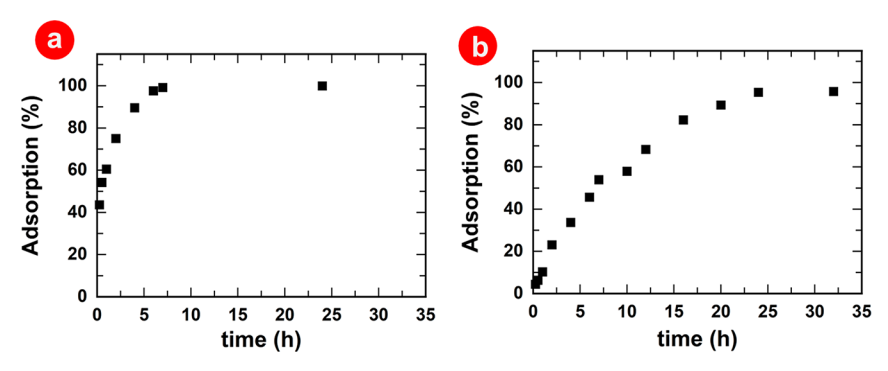
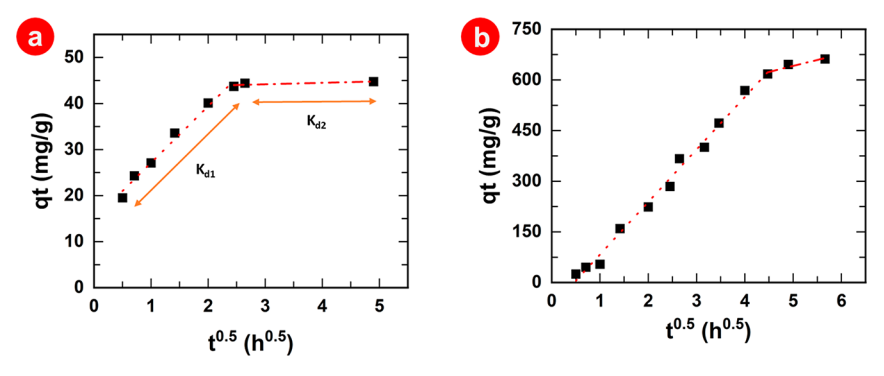


Figure 7. Removal performance of PSNPs with time onto 100 ppm of Cr-MOF at pH 5, T = 25 °C and with the initial concentrations of PSNPs (a) 5 ppm and (b) 70 ppm.

Table 2. Intraparticle Diffusion Model Parameters of Adsorption of PSNPs on Cr-MOF

	intraparticle diffusion parameters							
	$q_t = K_d t^{0.5} + C$							
conc. (ppm)	$K_{\rm d1}({\rm mg/g.h^{0.5}})$	$R^2$	$C_1(mg/g)$	$C_1$ (h <sup>0.5</sup> )	$K_{\rm d2}({\rm mg/g.h}^{0.5})$	$R^2$	$C_2(mg/g)$	$C_2$ (h <sup>0.5</sup> )
5	12.28	0.98	+14.87	-1.21	0.31	0.79	43.26	-140.14
70	155.53	0.99	-72.46	+0.47	35.57	0.9	463.55	-13.03



**Figure 8.** Intraparticle diffusion model fitting for adsorption of PSNPs onto 100 ppm of Cr-MOF at pH 5, temperature 25  $^{\circ}$ C, and with the initial concentration of PSNPs (a) 5 ppm and (b) 70 ppm.  $q_t$  is the transient adsorption capacity at time t.

# 3.3. Kinetics Analysis of the PSNPs Isotherms Adsorption on Cr-MOF

Kinetic experiments were performed to determine the pattern of adsorption between PSNPs and Cr-MOF. Among the two kinetics models, the pseudo-first-order kinetics showed a better fit to the experimental data in both cases of initial concentration of PSNPs with an  $R^2$  value of more than 0.9 (Table 1) (Figure S3). Based on the fitted model, and as it was discussed earlier, the physical adsorption mechanism (i.e., electrostatic interactions) was more dominating than chemical adsorption for the adsorption of PSNPs on Cr-MOF.<sup>31</sup> In addition, the FTIR analysis of Cr-MOF after adsorption (Figure 6a) did not show the formation of any new peaks or

shift in the peaks, suggesting no new chemical bonds were formed between Cr-MOF and PSNPs during the adsorption process.

Based on the pseudo-first-order model, the adsorption of 98% was obtained in 6 h for 5 ppm PSNPs and adsorption of 96% was obtained in 24 h in the case of 70 ppm PSNPs (Figure 7). The rate constant values  $(K_1, K_2)$  were higher at the lower initial concentrations (5 ppm) of PSNPs compared to the 70 ppm PSNPs. The faster adsorption at a low initial concentration of adsorbate was justified due to the higher active sites to adsorbate ratio.<sup>30</sup>

The adsorption process can typically be broken down into three separate phases. First, the adsorbate (PSNPs) is transported from the bulk liquid to the external surface of the adsorbent (Cr-MOF) (external mass transfer). Next, the adsorbate diffuses in the pores of the adsorbent (intraparticle diffusion), and interaction occurs inside the adsorbent and on the external surface (adsorption). The intraparticle diffusion model equation is mentioned in Table 2, in which  $q_t$  is the transient adsorption capacity at time t,  $K_d$  is the intraparticle diffusion rate constant, and C is the intercept that provides information about the boundary layer thickness. 71 The intercept value (C) is directly proportional to the thickness of the boundary layer, which means that, when the value of the time-intercept is larger, the effect of boundary layer thickness is larger.<sup>34</sup> Usually, the time-axis intercept is considered for the intraparticle diffusion study, but some literature has also reported the q-axis intercept. In this study, both time axis and q-axis intercepts are reported because positive values of both qaxis intercept and time axis intercept are obtained.

As shown in Figure 8, two distinct diffusion regions are obtained, which implies that more than one process influences the adsorption. The first area of the plot is assigned to the external mass transfer process, whereas the second region is assigned to the intraparticle diffusion process.  $^{72}$  The plots of  $q_t$ versus  $t^{0.5}$  do not pass through the origin, which states that intraparticle diffusion is not the only process that affects the adsorption rate. For both PSNPs concentrations, the higher  $K_{\rm d1}$  as compared with the  $K_{\rm d2}$  value suggests that the adsorption of PSNPs onto Cr-MOF took place at a faster rate through external mass transfer than intraparticle diffusion.<sup>30</sup> The  $K_{d1}$  value for 70 ppm initial concentration PSNPs is larger than that of 5 ppm initial concentration, suggesting a faster rate of external mass transfer in the case of 70 ppm due to the greater concentration gradients (active driving force). For the 5 ppm initial concentration of PSNPs, the negative time-axis intercept suggests a low boundary layer thickness effect and instantaneous adsorption. Whereas, for 70 ppm initial concentration of PSNPs, a positive time-axis intercept was obtained, which states a high boundary layer effect on adsorption. The 70 ppm initial concentration PSNPs required more time to achieve equilibrium as compared with the 5 ppm PSNPs, which might also be due to the higher effect of boundary layer thickness. Hence, it can be deduced that, at a higher adsorbate concentration, the boundary layer effects were more significant and determined the required time to reach equilibrium. Comparing  $K_{d1}$  and  $K_{d2}$  for both 5 and 70 ppm concentrations, it can be concluded that intraparticle diffusion (lower  $K_{d2}$  than  $K_{d1}$ ) is the rate-limiting step of the adsorption process.

#### 3.4. Isotherm Adsorption study

Equilibrium adsorption experiments were performed at the initial concentration of PSNPs ranging from 5–100 ppm, pH 5, temperature 25 °C, and 100 ppm of Cr-MOF, to study the effect of the initial concentration of PSNPs on adsorption. Three adsorption isotherm models, namely, Langmuir, Freundlich, and Temkin, were applied to fit the experimental data. The equilibrium adsorption capacity of Cr-MOF increased with the increasing initial concentration of PSNPs owing to the higher mass transfer (Figure 9). The maximum PSNPs concentration tested here is 90 ppm, which showed an increased adsorption capacity of 800 (mg/g). This increasing trend shows the potential of proposed Cr-MOF for the removal of PSNPs concentrations higher than 90 ppm. The fitting parameter values and correlation coefficient for

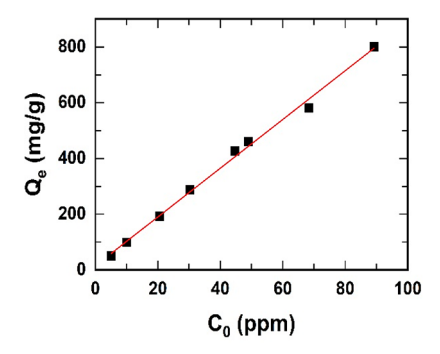


**Figure 9.** Effect of initial concentration of PSNPs on adsorption at pH 5, temperature 25  $^{\circ}$ C, and adsorption time of 24 h.  $Q_{e}$  is adsorption capacity at equilibrium.

Langmuir, Freundlich, and Temkin models are mentioned in Table 3 and Figure S4. The Freundlich model showed the best fitting, suggesting multilayer adsorption of PSNPs onto the surface of Cr-MOF and the heterogeneous surface of the adsorbent. The multilayer physical adsorption behavior can be supported based on the BET analysis results (Figure 2f) that showed that the pore size of Cr-MOF was ~3 nm and the particle size of PSNPs was ~65 nm (Figure 3b1,c1), stating no pore diffusion took place due to the small pore size of adsorbent. This also was suggested by the intraparticle diffusion model that diffusion of adsorbates into the MOF pores is the limiting adsorption step.

#### 3.5. Regeneration and Reusability

The desorption experiments were performed using sodium hydroxide, ethanol, and methanol for regenerating the Cr-MOF (Figure S5). NaOH and ethanol were selected for the regeneration due to the existence of hydroxide and ethoxide in their structure.<sup>73</sup> Based on the FTIR analysis (Figure S5a), both solvents could regenerate the Cr-MOF completely since no sign of PSNPs was observed and they provided almost similar adsorption efficiency in the second cycle. The NaOHregenerated Cr-MOF showed 85% adsorption, and the ethanol-regenerated Cr-MOF showed 75% adsorption in the second adsorption cycle (Figure S5b). Since both solvents showed complete desorption of PSNPs from the surface of the Cr-MOF (based on the FTIR data) and based on the fact that physisorption was the main adsorption mechanism, the reduction in adsorption should be due to physicochemical changes in the Cr-MOF during the regeneration process. Since higher efficiency was achieved using NaOH for the regeneration of MOFs in the second cycle, further adsorption-desorption cycles were performed using NaOH. The adsorption efficiency of regenerated Cr-MOF decreased from 91  $\pm$  4.3% for the first adsorption cycle to 81  $\pm$  15% for the second,  $79 \pm 16\%$  for the third adsorption cycle, and, finally, reduced to  $68 \pm 15\%$  for the fourth adsorption cycle as shown in Figure 10a. Cr-MOF showed acceptable adsorption loss ( $\sim$ 10%) for the third regeneration cycle and then showed around 10% more loss in the fourth regeneration. To investigate the possible reasons for the loss in adsorption after regeneration, the effect of water and NaOH on the MOF structure was explored.

To check the effect of water on the physicochemical stability of Cr-MOF, the Cr-MOF was immersed in water for 1 and 5 days, and the surface chemistry and crystal pattern of the MOFs were analyzed by FTIR and XRD. The FTIR of the water-immersed MOF showed no changes in the FTIR pattern

Table 3. Equilibrium Constants for Adsorption of PSNPs on Cr-MOF

Langmuir			Freundlich			Temkin		
$Q_e = \frac{Q_{\text{max}} K_L C_e}{1 + K_L C_e}$			$Q_{\rm e} = K_{\rm F} C_{\rm e}^{1/n}$			$Q_e = B \ln K_T + B \ln C_e$		
$Q_{\text{max}}(\text{mg/g})$	$K_{\rm L}({\rm L/mg})$	$R^2$	$K_{\rm F} \left( {\rm mg} (1-1/{\rm n}) {\rm L}^{1/{\rm n}} {\rm g}^{-1} \right)$	n	$R^2$	В	$K_{\mathrm{T}}(\mathrm{L/mg})$	$R^2$
319.49	6.91	0.86	251.91	2.16	0.97	115.93	20.14	0.80

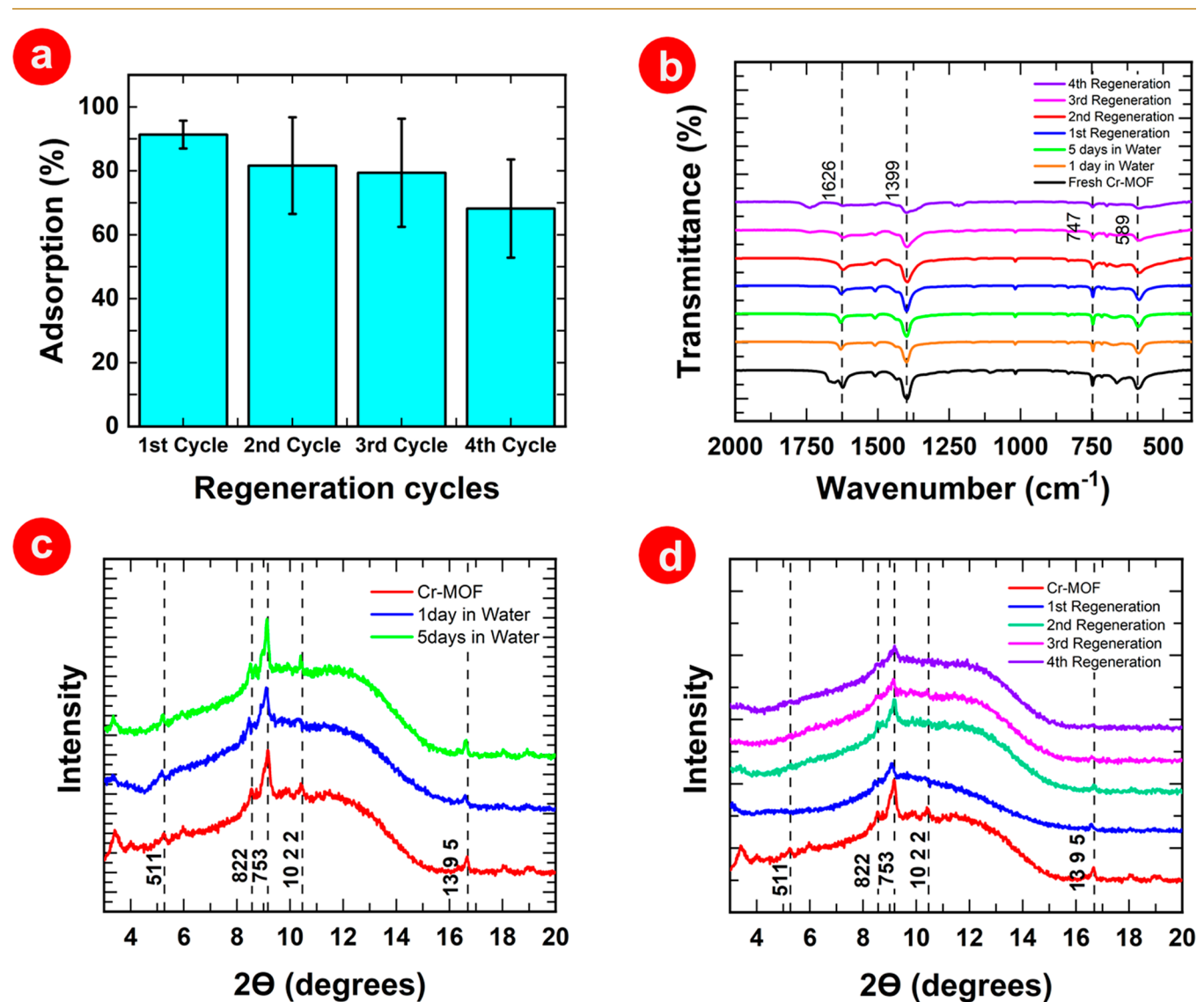


Figure 10. (a) Four cycle regeneration of Cr-MOF using NaOH for the removal of 5 ppm PSNPs using 100 ppm regenerated Cr-MOF. (b) FTIR analysis of water-immersed Cr-MOF for 1 and 5 days and regenerated Cr-MOF after every regeneration cycle. (c) XRD pattern of water-immersed Cr-MOF after 1 and 5 days. (d) XRD pattern of regenerated Cr-MOF using NaOH.

of Cr-MOF that confirmed that water did not change the surface chemistry of MOF (Figure 10b). The XRD results of Cr-MOF immersed in water for 1 and 5 days showed no change in crystallinity, stating the water did not affect the structure of MOFs (Figure 10c). However, the XRD analysis of Cr-MOF regenerated with NaOH after every adsorption—desorption cycle showed changes in the crystallinity of MOFs, including the elimination of peaks indexed as 511, 822, 1022, and 1395 and intensity reduction of height indexed as 753 (Figure 10d) due to the use of NaOH for regeneration. The elimination of peaks or lower intensity suggests the alteration of crystallinity, as the NaOH might have affected the structure

of Cr-MOF during regeneration.<sup>74</sup> The FTIR of regenerated MOFs showed lower intensity at all the representative wavenumbers 1626 (C=C), 1399 (O-C-O), 747 (C-H), and 589 cm<sup>-1</sup> (Cr-O), which might be because of the NaOH interaction with MOF during regeneration and alteration of these bonds.

In addition to the change in MOF structure during the regeneration, the lower adsorption of regenerated MOF might be due to the change in size and surface charge of MOF. The z-average size of Cr-MOF after regeneration with ethanol and NaOH was obtained as  $1434 \pm 618$  and  $3442 \pm 1808$  nm, respectively. The increased size of Cr-MOF after regeneration

compared to the fresh Cr-MOF size (400–600 nm) (Figure 3a1,a2) might be the reason for the lower adsorption performance of Cr-MOF after regeneration because the aggregated MOF provided less adsorption active sites. In addition, a lowered  $\zeta$  potential of regenerated Cr-MOF with both solvents of ethanol (ZP = +14.2) and NaOH (ZP = +2.66) was observed as compared to the  $\zeta$  potential (ZP = +20 at pH = 5) of fresh MOF (Figure 3a1). Since electrostatic interaction was the dominant adsorption mechanism, the decreased  $\zeta$  potential might be another reason for the lower adsorption performance in the second adsorption cycle. Methanol as a regeneration solvent resulted in MOFs, which could provide only 60% adsorption. Considering methanol is a toxic solvent and owing to its lower regeneration efficiency, methanol was found not to be a suitable regenerator solvent.<sup>73</sup>

#### 4. CONCLUSION

This work investigated the adsorption capacity and removal efficiency of polystyrene nanoplastics (PSNPs) from water using Cr-MOF as well as the effect of different experimental conditions on the adsorption capacity. It was found that the removal of PSNPs is mainly dominated by electrostatic attraction between negatively charged PSNPs and positively charged Cr-MOF, and about 96% removal was obtained at both 5 and 70 ppm initial concentration of PSNPs. Cr-MOF was successfully synthesized by the solvothermal method and showed promising potential with an enhanced affinity toward PSNPs. The highest removal efficiency of PSNPs was obtained at pH 5, whereas negligible removal was obtained at pH 10. The experimental data showed that the pseudo-first-order kinetics model is a better fit, stating the physical adsorption of PSNPs on Cr-MOF. The adsorption capacity of Cr-MOF significantly increased with an increasing initial concentration of PSNPs, and a maximum adsorption capacity of 800 mg/g was achieved. The isotherm study showed a better fit for the Freundlich adsorption model, suggesting the heterogeneous nature of the adsorption of PSNPs on Cr-MOF. The regeneration of MOFs with ethanol and sodium hydroxide showed complete desorption of PSNPs from the surface of Cr-MOFs; however, the regenerated MOFs showed lower adsorption performance.

#### ASSOCIATED CONTENT

#### Supporting Information

The Supporting Information is available free of charge at https://pubs.acs.org/doi/10.1021/acsaenm.2c00174.

Discussion of XRD analysis and figures of XRD pattern, EDX/EDS analysis, kinetics model fitting, equilibrium isotherm data fitting, and FTIR analysis (PDF)

#### AUTHOR INFORMATION

# **Corresponding Author**

Milad Rabbani Esfahani — Department of Chemical and Biological Engineering, University of Alabama, Tuscaloosa, Alabama 35487, United States; orcid.org/0000-0001-6530-4310; Phone: 205-348-8836; Email: mesfahani@eng.ua.edu

#### **Authors**

Sweta Modak — Department of Chemical and Biological Engineering, University of Alabama, Tuscaloosa, Alabama 35487, United States

Medha Kasula – Department of Chemical and Biological Engineering, University of Alabama, Tuscaloosa, Alabama 35487, United States

Complete contact information is available at: https://pubs.acs.org/10.1021/acsaenm.2c00174

#### **Notes**

The authors declare no competing financial interest.

#### ACKNOWLEDGMENTS

The authors wish to acknowledge the National Science Foundation (NSF) for financial support under NSF award number CBET-1941700. The authors also acknowledge the support received from the Alabama Water Institute and the Chemical and Biological Engineering Department at The University of Alabama. The authors thank Dr. James Shogren-Harris for the BET analysis.

#### REFERENCES

- (1) Andrady, A. L.; Neal, M. A. Applications and societal benefits of plastics. *Philos. Trans R Soc. Lond B Biol. Sci.* **2009**, 364 (1526), 1977–1984.
- (2) Ivleva, N. P.; Wiesheu, A. C.; Niessner, R. Microplastic in Aquatic Ecosystems. *Angew. Chem., Int. Ed.* **2017**, *56* (7), 1720–1739. (3) Harris, P. T.; Tamelander, J.; Lyons, Y.; Neo, M. L.; Maes, T. Taking a mass-balance approach to assess marine plastics in the South China Sea. *Mar. Pollut. Bull.* **2021**, *171*, 112708.
- (4) Kaza, S.; Yao, L. C.; Bhada-Tata, P.; Van Woerden, F.What a Waste 2.0: A Global Snapshot of Solid Waste Management to 2050; World Bank: Washington, DC, 2018.
- (5) Duis, K.; Coors, A. Microplastics in the aquatic and terrestrial environment: sources (with a specific focus on personal care products), fate and effects. *Environmental Sciences Europe* **2016**, 28 (1), 2.
- (6) Hernandez, L. M.; Yousefi, N.; Tufenkji, N. Are There Nanoplastics in Your Personal Care Products? *Environ. Sci. Technol. Lett.* **2017**, 4 (7), 280–285.
- (7) Gigault, J.; Pedrono, B.; Maxit, B.; Ter Halle, A. Marine plastic litter: the unanalyzed nano-fraction. *Environmental Science: Nano* **2016**, 3 (2), 346–350.
- (8) Akdogan, Z.; Guven, B. Microplastics in the environment: A critical review of current understanding and identification of future research needs. *Environ. Pollut.* **2019**, 254, 113011.
- (9) Browne, M. A.; Crump, P.; Niven, S. J.; Teuten, E.; Tonkin, A.; Galloway, T.; Thompson, R. Accumulation of Microplastic on Shorelines Woldwide: Sources and Sinks. *Environ. Sci. Technol.* **2011**, *45* (21), 9175–9179.
- (10) Kannan, K.; Vimalkumar, K. A Review of Human Exposure to Microplastics and Insights Into Microplastics as Obesogens. *Front Endocrinol (Lausanne)* **2021**, *12*, 724989.
- (11) Wang, T.; Yu, C.; Chu, Q.; Wang, F.; Lan, T.; Wang, J. Adsorption behavior and mechanism of five pesticides on microplastics from agricultural polyethylene films. *Chemosphere* **2020**, 244, 125491.
- (12) Li, J.; Zhang, K.; Zhang, H. Adsorption of antibiotics on microplastics. *Environ. Pollut.* **2018**, 237, 460–467.
- (13) Yan, W.; Hamid, N.; Deng, S.; Jia, P. P.; Pei, D. S. Individual and combined toxicogenetic effects of microplastics and heavy metals (Cd, Pb, and Zn) perturb gut microbiota homeostasis and gonadal development in marine medaka (Oryzias melastigma). *J. Hazard Mater.* **2020**, 397, 122795.

- (14) Gaylarde, C. C.; Baptista Neto, J. A.; da Fonseca, E. M. Nanoplastics in aquatic systems are they more hazardous than microplastics? *Environ. Pollut.* **2021**, 272, 115950.
- (15) Kundu, A.; Shetti, N. P.; Basu, S.; Reddy, K. R.; Nadagouda, M. N.; Aminabhavi, T. M. Identification and removal of micro- and nanoplastics: Efficient and cost-effective methods. *Chem. Eng. J.* **2021**, 421 (1), 129816.
- (16) Campanale; Massarelli; Savino; Locaputo; Uricchio. A Detailed Review Study on Potential Effects of Microplastics and Additives of Concern on Human Health. *International Journal of Environmental Research and Public Health* **2020**, 17 (4), 1212.
- (17) Ramasamy, B. S. S.; Palanisamy, S. A review on occurrence, characteristics, toxicology and treatment of nanoplastic waste in the environment. *Environ. Sci. Pollut Res. Int.* **2021**, 28 (32), 43258–43273.
- (18) Revel, M.; Châtel, A.; Mouneyrac, C. Micro(nano)plastics: A threat to human health? Current Opinion in Environmental Science & Health 2018, 1, 17–23.
- (19) Kik, K.; Bukowska, B.; Sicinska, P. Polystyrene nanoparticles: Sources, occurrence in the environment, distribution in tissues, accumulation and toxicity to various organisms. *Environ. Pollut.* **2020**, 262, 114297.
- (20) Liu, J.; Ma, Y.; Zhu, D.; Xia, T.; Qi, Y.; Yao, Y.; Guo, X.; Ji, R.; Chen, W. Polystyrene Nanoplastics-Enhanced Contaminant Transport: Role of Irreversible Adsorption in Glassy Polymeric Domain. *Environ. Sci. Technol.* **2018**, 52 (5), 2677–2685.
- (21) Liu, J.; Zhang, T.; Tian, L.; Liu, X.; Qi, Z.; Ma, Y.; Ji, R.; Chen, W. Aging Significantly Affects Mobility and Contaminant-Mobilizing Ability of Nanoplastics in Saturated Loamy Sand. *Environ. Sci. Technol.* **2019**, 53 (10), 5805–5815.
- (22) Turner, A. Foamed Polystyrene in the Marine Environment: Sources, Additives, Transport, Behavior, and Impacts. *Environ. Sci. Technol.* **2020**, *54* (17), 10411–10420.
- (23) Shams, M.; Alam, I.; Chowdhury, I. Aggregation and stability of nanoscale plastics in aquatic environment. *Water Res.* **2020**, *171*, 115401.
- (24) Bayo, J.; Lopez-Castellanos, J.; Olmos, S. Membrane bioreactor and rapid sand filtration for the removal of microplastics in an urban wastewater treatment plant. *Mar. Pollut. Bull.* **2020**, *156*, 111211.
- (25) Lagarde, F.; Olivier, O.; Zanella, M.; Daniel, P.; Hiard, S.; Caruso, A. Microplastic interactions with freshwater microalgae: Hetero-aggregation and changes in plastic density appear strongly dependent on polymer type. *Environ. Pollut.* **2016**, *215*, 331–339.
- (26) Lares, M.; Ncibi, M. C.; Sillanpaa, M.; Sillanpaa, M. Occurrence, identification and removal of microplastic particles and fibers in conventional activated sludge process and advanced MBR technology. *Water Res.* **2018**, *133*, 236–246.
- (27) Perren, W.; Wojtasik, A.; Cai, Q. Removal of Microbeads from Wastewater Using Electrocoagulation. *ACS Omega* **2018**, 3 (3), 3357–3364.
- (28) Sturm, M. T.; Horn, H.; Schuhen, K. Removal of Microplastics from Waters through Agglomeration-Fixation Using Organosilanes—Effects of Polymer Types, Water Composition and Temperature. *Water* **2021**, *13* (5), 675.
- (29) Padervand, M.; Lichtfouse, E.; Robert, D.; Wang, C. Removal of microplastics from the environment. A review. *Environmental Chemistry Letters* **2020**, *18* (3), 807–828.
- (30) Arenas, L. R.; Gentile, S. R.; Zimmermann, S.; Stoll, S. Nanoplastics adsorption and removal efficiency by granular activated carbon used in drinking water treatment process. *Sci. Total Environ.* **2021**, 791, 148175.
- (31) Zhou, G.; Huang, X.; Xu, H.; Wang, Q.; Wang, M.; Wang, Y.; Li, Q.; Zhang, Y.; Ye, Q.; Zhang, J. Removal of polystyrene nanoplastics from water by CuNi carbon material: The role of adsorption. *Sci. Total Environ.* **2022**, *820*, 153190.
- (32) Tiwari, E.; Singh, N.; Khandelwal, N.; Monikh, F. A.; Darbha, G. K. Application of Zn/Al layered double hydroxides for the removal of nano-scale plastic debris from aqueous systems. *J. Hazard Mater.* **2020**, 397, 122769.

- (33) Yuan, S.; Feng, L.; Wang, K.; Pang, J.; Bosch, M.; Lollar, C.; Sun, Y.; Qin, J.; Yang, X.; Zhang, P.; Wang, Q.; Zou, L.; Zhang, Y.; Zhang, L.; Fang, Y.; Li, J.; Zhou, H. C. Stable Metal-Organic Frameworks: Design, Synthesis, and Applications. *Adv. Mater.* **2018**, 30 (37), 1704303.
- (34) Kasula, M.; Le, T.; Thomsen, A.; Rabbani Esfahani, M. Silver metal organic frameworks and copper metal organic frameworks immobilized on graphene oxide for enhanced adsorption in water treatment. *Chem. Eng. J.* **2022**, *439*, 135542.
- (35) Le, T.; Chen, X.; Dong, H.; Tarpeh, W.; Perea-Cachero, A.; Coronas, J.; Martin, S. M.; Mohammad, M.; Razmjou, A.; Esfahani, A. R.; Koutahzadeh, N.; Cheng, P.; Kidambi, P. R.; Esfahani, M. R. An Evolving Insight into Metal Organic Framework-Functionalized Membranes for Water and Wastewater Treatment and Resource Recovery. *Ind. Eng. Chem. Res.* **2021**, *60* (19), 6869–6907.
- (36) Dai, R.; Guo, H.; Tang, C. Y.; Chen, M.; Li, J.; Wang, Z. Hydrophilic Selective Nanochannels Created by Metal Organic Frameworks in Nanofiltration Membranes Enhance Rejection of Hydrophobic Endocrine-Disrupting Compounds. *Environ. Sci. Technol.* **2019**, 53 (23), 13776–13783.
- (37) Dai, R.; Wang, X.; Tang, C. Y.; Wang, Z. Dually Charged MOF-Based Thin-Film Nanocomposite Nanofiltration Membrane for Enhanced Removal of Charged Pharmaceutically Active Compounds. *Environ. Sci. Technol.* **2020**, *54* (12), 7619–7628.
- (38) Liu, K.; Yu, M.; Wang, H.; Wang, J.; Liu, W.; Hoffmann, M. R. Multiphase Porous Electrochemical Catalysts Derived from Iron-Based Metal-Organic Framework Compounds. *Environ. Sci. Technol.* **2019**, 53 (11), 6474–6482.
- (39) Zhang, Y.; Yuan, S.; Feng, X.; Li, H.; Zhou, J.; Wang, B. Preparation of Nanofibrous Metal-Organic Framework Filters for Efficient Air Pollution Control. J. Am. Chem. Soc. 2016, 138 (18), 5785–5788.
- (40) Liu, K.; Zhang, S.; Hu, X.; Zhang, K.; Roy, A.; Yu, G. Understanding the Adsorption of PFOA on MIL-101(Cr)-Based Anionic-Exchange Metal-Organic Frameworks: Comparing DFT Calculations with Aqueous Sorption Experiments. *Environ. Sci. Technol.* **2015**, 49 (14), 8657–8665.
- (41) Li, R.; Alomari, S.; Islamoglu, T.; Farha, O. K.; Fernando, S.; Thagard, S. M.; Holsen, T. M.; Wriedt, M. Systematic Study on the Removal of Per- and Polyfluoroalkyl Substances from Contaminated Groundwater Using Metal-Organic Frameworks. *Environ. Sci. Technol.* **2021**, 55 (22), 15162–15171.
- (42) Chen, Y.-J.; Chen, Y.; Miao, C.; Wang, Y.-R.; Gao, G.-K.; Yang, R.-X.; Zhu, H.-J.; Wang, J.-H.; Li, S.-L.; Lan, Y.-Q. Metal-organic framework-based foams for efficient microplastics removal. *Journal of Materials Chemistry A* **2020**, 8 (29), 14644–14652.
- (43) Wan, H.; Wang, J.; Sheng, X.; Yan, J.; Zhang, W.; Xu, Y. Removal of Polystyrene Microplastics from Aqueous Solution Using the Metal-Organic Framework Material of ZIF-67. *Toxics* **2022**, *10* (2), 70.
- (44) Far, H. S.; Hasanzadeh, M.; Najafi, M.; Nezhad, T. R. M.; Rabbani, M. Efficient Removal of Pb(II) and Co(II) Ions from Aqueous Solution with a Chromium-Based Metal-Organic Framework/Activated Carbon Composites. *Ind. Eng. Chem. Res.* **2021**, *60* (11), 4332–4341.
- (45) Langmuir, I. The adsorption of gases on plane surfaces of glass, mica and platinum. *J. Am. Chem. Soc.* **1918**, 40 (9), 1361–1403.
- (46) Freundlich, H. Over the adsorption in solution. *J. Phys. Chem.* **1906**, 57, 1100–1107.
- (47) Araújo, C. S. T.; Almeida, I. L. S.; Rezende, H. C.; Marcionilio, S. M. L. O.; Léon, J. J. L.; de Matos, T. N. Elucidation of mechanism involved in adsorption of Pb(II) onto lobeira fruit (Solanum lycocarpum) using Langmuir, Freundlich and Temkin isotherms. *Microchemical Journal* **2018**, *137*, 348–354.
- (48) Alkurdi, S. S. A.; Al-Juboori, R. A.; Bundschuh, J.; Bowtell, L.; Marchuk, A. Inorganic arsenic species removal from water using bone char: A detailed study on adsorption kinetic and isotherm models using error functions analysis. *J. Hazard Mater.* **2021**, *405*, 124112.

- (49) Matouq, M.; Jildeh, N.; Qtaishat, M.; Hindiyeh, M.; Al Syouf, M. Q. The adsorption kinetics and modeling for heavy metals removal from wastewater by Moringa pods. *Journal of Environmental Chemical Engineering* **2015**, 3 (2), 775–784.
- (50) Jiang, S.; Yu, T.; Xia, R.; Wang, X.; Gao, M. Realization of super high adsorption capability of 2D  $\delta$ -MnO $_2$  /GO through intra-particle diffusion. *Mater. Chem. Phys.* **2019**, 232, 374–381.
- (51) Shen, B.; Chen, X.; Shen, K.; Xiong, H.; Wei, F. Imaging the node-linker coordination in the bulk and local structures of metalorganic frameworks. *Nat. Commun.* **2020**, *11* (1), 2692.
- (52) Celeste, A.; Paolone, A.; Itie, J. P.; Borondics, F.; Joseph, B.; Grad, O.; Blanita, G.; Zlotea, C.; Capitani, F. Mesoporous Metal-Organic Framework MIL-101 at High Pressure. *J. Am. Chem. Soc.* **2020**, *142* (35), 15012–15019.
- (53) Zhang, L. J.; Li, F. Q.; Ren, J. X.; Ma, L. B.; Li, M. Q. Preparation of metal organic frameworks MIL-101 (Cr) with acetic acid as mineralizer. *IOP Conf. Ser.: Earth Environ. Sci.* **2018**, 199, 042038.
- (54) Manteghi, F.; Zakeri, F.; Guy, O. J.; Tehrani, Z. MIL-101(Cr), an Efficient Heterogeneous Catalyst for One Pot Synthesis of 2,4,5-tri Substituted Imidazoles under Solvent Free Conditions. *Nanomaterials* (*Basel*) 2021, 11 (4), 845.
- (55) Ramos-Fernandez, E. V.; Pieters, C.; van der Linden, B.; Juan-Alcañiz, J.; Serra-Crespo, P.; Verhoeven, M. W. G. M.; Niemantsverdriet, H.; Gascon, J.; Kapteijn, F. Highly dispersed platinum in metal organic framework NH2-MIL-101(Al) containing phosphotungstic acid Characterization and catalytic performance. *J. Catal.* 2012, 289, 42–52.
- (56) Du, P. D.; Thanh, H. T. M.; To, T. C.; Thang, H. S.; Tinh, M. X.; Tuyen, T. N.; Hoa, T. T.; Khieu, D. Q. Metal-Organic Framework MIL-101: Synthesis and Photocatalytic Degradation of Remazol Black B Dye. *J. Nanomater.* **2019**, 2019, 1–15.
- (57) Zhou, F.; Zhou, J.; Gao, X.; Kong, C.; Chen, L. Facile synthesis of MOFs with uncoordinated carboxyl groups for selective CO<sub>2</sub> capture via postsynthetic covalent modification. *RSC Adv.* **2017**, 7 (7), 3713–3719.
- (58) Huang, X.; Hu, Q.; Gao, L.; Hao, Q.; Wang, P.; Qin, D. Adsorption characteristics of metal-organic framework MIL-101(Cr) towards sulfamethoxazole and its persulfate oxidation regeneration. *RSC Adv.* **2018**, *8* (49), 27623–27630.
- (59) Thi Thanh Chau, V.; Thi MinhThanh, H.; Dinh Du, P.; Thanh Tam Toan, T.; Ngoc Tuyen, T.; Xuan Mau, T.; Quang Khieu, D. Metal-Organic Framework-101 (MIL-101): Synthesis, Kinetics, Thermodynamics, and Equilibrium Isotherms of Remazol Deep Black RGB Adsorption. *J. Chem.* 2018, 2018, 1–14.
- (60) Quan, X.; Sun, Z.; Meng, H.; Han, Y.; Wu, J.; Xu, J.; Xu, Y.; Zhang, X. Surface functionalization of MIL-101(Cr) by aminated mesoporous silica and improved adsorption selectivity toward special metal ions. *Dalton Trans* **2019**, 48 (16), 5384–5396.
- (61) Jia, Y.; Duran, C.; Hotta, Y.; Sato, K.; Watari, K. The-effect-of-polyelectrolyte-on-fabrication of macroporous ZrO<sub>2</sub> ceramics. *J. Mater. Sci.* **2005**, *40*, 2903–2909.
- (62) Al-Gebory, L.; Mengüç, M. P. The effect of pH on particle agglomeration and optical properties of nanoparticle suspensions. *Journal of Quantitative Spectroscopy and Radiative Transfer* **2018**, 219, 46–60.
- (63) Hasan, Z.; Jhung, S. H. Removal of hazardous organics from water using metal-organic frameworks (MOFs): plausible mechanisms for selective adsorptions. *J. Hazard Mater.* **2015**, 283, 329–339.
- (64) Yan, X.; Yang, Y.; Wang, C.; Hu, X.; Zhou, M.; Komarneni, S. Surfactant-assisted synthesis of ZIF-8 nanocrystals for phthalic acid adsorption. *J. Sol-Gel Sci. Technol.* **2016**, *80* (2), 523–530.
- (65) Huo, S. H.; Yan, X. P. Facile magnetization of metal-organic framework MIL-101 for magnetic solid-phase extraction of polycyclic aromatic hydrocarbons in environmental water samples. *Analyst* **2012**, 137 (15), 3445–3451.
- (66) Lu, N.; Wang, T.; Zhao, P.; Zhang, L.; Lun, X.; Zhang, X.; Hou, X. Experimental and molecular docking investigation on metal-organic framework MIL-101(Cr) as a sorbent for vortex assisted dispersive

- micro-solid-phase extraction of trace 5-nitroimidazole residues in environmental water samples prior to UPLC-MS/MS analysis. *Anal Bioanal Chem.* **2016**, *408* (29), 8515–8528.
- (67) Agboola, O. D.; Benson, N. U. Physisorption and Chemisorption Mechanisms Influencing Micro (Nano) Plastics-Organic Chemical Contaminants Interactions: A Review. Front. Environ. Sci. 2021, 9, 678574.
- (68) Chakraborty, D.; Naik, S.; Kumar, S.; Chandrasekaran, N.; Mukherjee, A. Exploring the interactions between protein coronated CdSe quantum dots and nanoplastics. *New J. Chem.* **2021**, *45* (18), 7951–7958.
- (69) Kayal, S.; Chakraborty, A. Activated carbon (type Maxsorb-III) and MIL-101(Cr) metal organic framework based composite adsorbent for higher CH<sub>4</sub> storage and CO<sub>2</sub> capture. *Chem. Eng. J.* **2018**, 334, 780–788.
- (70) Karmakar, S.; Roy, D.; Janiak, C.; De, S. Insights into multi-component adsorption of reactive dyes on MIL-101-Cr metal organic framework: Experimental and modeling approach. *Sep. Purif. Technol.* **2019**, 215, 259–275.
- (71) Luo, X.-P.; Fu, S.-Y.; Du, Y.-M.; Guo, J.-Z.; Li, B. Adsorption of methylene blue and malachite green from aqueous solution by sulfonic acid group modified MIL-101. *Microporous Mesoporous Mater.* **2017**, 237, 268–274.
- (72) Wu, F.-C.; Tseng, R.-L.; Juang, R.-S. Initial behavior of intraparticle diffusion model used in the description of adsorption kinetics. *Chem. Eng. J.* **2009**, *153* (1–3), 1–8.
- (73) Larasati, A.; Fowler, G. D.; Graham, N. J. D. Chemical regeneration of granular activated carbon: preliminary evaluation of alternative regenerant solutions. *Environmental Science: Water Research & Technology* **2020**, *6* (8), 2043–2056.
- (74) Chen, C.; Zhang, M.; Guan, Q.; Li, W. Kinetic and thermodynamic studies on the adsorption of xylenol orange onto MIL-101(Cr). *Chem. Eng. J.* **2012**, *183*, 60–67.